Journal of Applied Fluid Mechanics, Vol. 17, No. 9, pp. 1938-1954, 2024.
Available online at www.jafmonline.net, ISSN 1735-3572, EISSN 1735-3645.
https://doi.org/10.47176/jafm.17.9.2550

Experimental and LES Studies of Propane–air Premixed Gases in Pipelines Containing Mixed Obstacles

Y. Wu[1,2], J. Gao[1,3,4†], Y. Han[1], B. Ai[1,2], X. Shao[1,2], B. Guo[1]and B. Hao[5]

[1] *School of Petrochemical Engineering & Environment, Zhejiang Ocean University, Zhoushan, 316022, China*
[2] *School of Naval Architecture & Maritime, Zhejiang Ocean University, Zhoushan, 316022, China*
[3] *National & Local Joint Engineering Research Center of Harbor Oil & Gas Storage and Transportation Technology, Zhoushan, 316022, China*
[4] *Zhejiang Key Laboratory of Petrochemical Environmental Pollution Control, Zhoushan, 316022, China*
[5] *Sinochem Zhoushan Hazardous Chemicals Emergency Rescue Base CO, LTD, Zhoushan 316021, China*

†Corresponding Author Email: gaojf409@zjou.edu.cn

ABSTRACT

This study investigated the effect of a mixed obstacle layout on the deflagration mechanism of propane–air premixed gases. Most previous studies focused on a single type of obstacle, changing the shape and number of the obstacles to observe the effect on the flame deflagration characteristics. However, in real explosion accident sites, obstacles are often a mixture of different types. Little literature exists on the deflagration characteristics of hybrid barriers in semi-confined spaces. In this paper, the deflagration characteristics of propane-air premixed gas with a mixed structure of hurdles and square obstacles was studied. First, the effectiveness of numerical simulations was demonstrated by comparing experimental and large eddy simulation (LES) results for the flame dynamics with a single flat plate obstacle. Based on this, the flame behavior for different layouts of square obstacles in a mixed obstacle configuration was further simulated using the large eddy simulation method, focusing on the flame behavior, overpressure characteristics, and flow field structure in the vicinity of the obstacle. The results showed that a mixed obstacle promoted flame evolution more than a single obstacle when the square obstacle was within a critical distance from the ignition source location at the same moment in time. When the flame front crossed the first hurdle-type obstacle, the flame pattern spread in a "cat's paw" pattern to the unburned portion of the tube. In addition, the increased distance of the square obstacle from the ignition source did not allow the peak overpressure and the peak rate of overpressure rise to show a positive feedback mechanism. Finally, the strength of the vorticity in the flow field was positively correlated with the distance of the square obstacle from the ignition source. The results of study provide theoretical for the prevention of explosions.

Article History

Received January 3, 2024
Revised March 10, 2024
Accepted March 19, 2024
Available online July 2, 2024

Keywords:

Overpressure characteristics
Flow field structure
Hurdle-type obstacles
Peak overpressure
Eddy quantity

1. INTRODUCTION

With the continuous growth of global energy demand, the mining rate of all kinds of energy minerals continues to increase, leading to occasional mineral mining explosions (He et al., 2019; Ismail et al., 2021; Yang et al., 2022; Baraza et al., 2023). To avoid explosions in long and narrow confined spaces, it is particularly important to study the factors that cause explosions in such spaces. There are many factors affecting the occurrence of explosions, including gas factors (Li et al., 2022a; Zhang et al., 2022; Wang et al., 2023a), the shape of the obstacle (Cheng et al., 2020; Wang & Ma, 2021b; Luo et al., 2022; Xiu et al., 2023a), and the way the obstacles are laid out (Lv et al.,2016; Zhao et al., 2022). The study of various types of factors is of great significance in the prevention of semi-confined space explosions that occur in real life. Propane is widely used in energy, industry, and chemical sectors due to its status as a clean energy source (Raj et al., 2023).

The impact of obstacles on deflagration characteristics and the original flow field (Bo et al., 2023; Cao et al., 2022) in a semi-confined space is indisputable. The flame interacts with the obstacle upon contact, leading

NOMENCLATURE

c	reaction progress variable	S_h	cumulative heat source term
dp/dt	overpressure growth rate	t	time
E	sum of the internal, kinetic, and potential energies of a fluid	T	temperature
f	unit mass force	t_{eff}	viscous stress component
h_j	enthalpy	u	velocity
J_j	diffusion flux	u_{eff}	effective viscosity
k_{eff}	jet velocity	ρ	density
p	pressure	$\overline{\quad}$	quantities filtered by physical space filters
S_c	reaction progress source term	$\tilde{\quad}$	the amount filtered by the Favre filter
S_{ceff}	effective Schmidt number	$\vec{\quad}$	vectors

to significant changes in the frontal area, propagation speed, explosion pressure, and flow field around the flame as it passes through the obstacle (Xiu et al., 2023b; Yang et al., 2024).

Flames propagating in a semi-confined barrier pipe are distorted due to the Rayleigh–Taylor (R-T) (Shen et al., 2019; Kagan & Sivashinsky, 2023) instability. The Kelvin–Helmholtz (K-H) instability based on the relative velocity of the fluid, however, has a greater impact on the flame front (Ponizy et al., 2014).

Based on the understanding of these two types of instability, changes in density gradient and pressure gradient in the tube significantly impact the combustion field and flow within the entire detonation space. It is also this change in gradient that ultimately leads to differences in vorticity strength within the tube. It has been shown that the shape of obstacles significantly influences the flame combustion characteristics and the vortex structure in the flow field during deflagration (Wang & Ma, 2021a; Zhang et al., 2021). During flame propagation, the flame is easily disturbed by obstacles to form different flame shapes. With the same obstruction rate, grids of square obstacles and porous circular obstacles split the flame, resulting in several strips of different sizes propagating forward. The flame will be disturbed by a single-hole circular obstacle, first forming a single cylinder and then dispersing in the form of a flare (Wang et al., 2022a).

Different types of obstacles also impact the rate at which the flame spreads, the highest explosion pressure, and the vorticity in space. The presence of obstacles and pipe walls can disturb the pressure wave inside the pipe during an explosion, which can enhance the degree of turbulence during deflagration and further promote flame combustion. Kindracki et al. (2007) studied the deflagration characteristics of methane–air mixtures in different types of closed containers with and without obstacles and with different ignition positions. The results showed that in pipelines with large aspect ratios, the presence of obstructions was more likely to affect the flame deflagration characteristics. Studies have shown that square obstacles promote flame propagation more than round obstacles when conditions are uniform (Qin et al., 2012). Correspondingly the speed and the maximum overpressure of a flame passing through a square obstacle were greater than those when passing through a circular obstacle. Porous obstacles are more likely to disrupt the blast flow field than baffle obstacles such as squares and circles. More vortices are likely to be generated.

The manner in which the obstacles are laid out (Gao et al., 2022; Lv et al., 2016) affects the characteristics of flame deflagration to some extent. Variations in the arrangement of obstacles during an explosion can impact the speed at which the flame spreads. The explosion pressure in the tube and the number of vortices (Xiu et al., 2023a) in the flow field also vary with the way the obstacles are laid out. To analyze the relationship between the consequences of explosions in semi-confined spaces and various influencing factors, scholars around the world have conducted a series of studies. Na'inna et al. (2015) experimentally explored the combustion characteristics and overpressure of methane-air mixed gas with different numbers of obstacles and different distances between obstacles. It was found that for the same number of obstacles, the explosion intensity was at its maximum when obstacles were placed with a suitable spacing from each other. Han et al. (2020) investigated the deflagration of a syngas-air mixture with varied hydrogen volume fractions by adjusting the position of obstacles in a closed pipeline. The experimental data revealed neither a positive nor a negative association between different obstacle positions and flame acceleration. Obstacles should be avoided in real-world environments for such conditions, and there is also some guidance on the use of syngas in complex environments.

Wang et al. (2022b) experimentally investigated the deflagration of premixed hydrogen in tubes under obstructions with different blockage rates. The maximum overpressure peak and the rate at which it was reached both increased in conjunction with an increase in the obstruction blocking rate. Furthermore, Na'inna et al. (2014) experimentally explored the deflagration of gas under two conditions: a single orifice plate obstruction but with different obstruction rates and two orifice plate obstructions with the same obstruction rate but with different spacings between the obstructions. It was found that the explosion intensity was greatest at a single obstacle obstruction rate of 0.4. When the distance between two obstacles, both with a blockage rate of 0.4, was at a suitable spacing, the maximum explosion overpressure and flame propagation velocity were twice as high as those for a single obstacle with a blockage rate of 0.4. In addition, Liu et al. (2023) studied the effect of the shape and arrangement of fence-type barriers on stoichiometric-specific hydroxide mixture combustion. The researchers focused on studying the process of flame acceleration and the transition from deflagration to detonation caused by obstacles (Goodwin et al., 2016).

occurrence during deflagration. It was found that rectangular obstacles were more likely to induce DDT (Saeid et al., 2021) than triangular obstacles under conditions of high obstruction rates. Under low-obstruction-rate conditions, triangular obstacle acceleration promoted flame acceleration more than rectangular obstacle acceleration. This study was instructive for the arrangement of obstacles in real complex environments.

With the development of computers and the development and upgrading of simulation software, a large number of researchers have used numerical simulations (Korytchenko et al., 2022; Signetti et al., 2023) in combination with experiments. Simulations predict the entire process of deflagration, and experiments are used to validate the simulations. The combination of the two has overcome many problems in the field of deflagration, but this process has lagged due to immature technology. For example, Yu et al. (2016) conducted a study examining the flame deflagration properties of barriers with varying cross-sectional shapes in the presence of gas through numerical simulations. The numerical findings indicated that the velocity, explosion overpressure, and turbulence intensity experienced during deflagration were significantly influenced by hollow triangular obstacles, while being minimally impacted by hollow circular obstacles at a specific coverage level.

Furthermore, Sheng et al. (2023) explored the flow field characteristics after deflagration under different obstacle layouts in a closed pipeline using the large eddy simulation method. They found that the central-type obstacle best facilitated flame propagation, maximizing the explosive overpressure throughout. When the ratio of the two instabilities (Ciccarelli et al., 2019; Li et al., 2021a), the R-T and K-H instabilities, reached a certain value, the center-type and peripheral-type obstacles had the most significant impact on the stability of the entire deflagration process. Because complex environments such as mines are prone to containing uneven obstacles, this study helped to circumvent the risk of combustible gas explosions in long, narrow, semi-enclosed spaces that are exacerbated by the improper layout of barriers.

On this basis, Chen et al. (2017) developed a subgrid-scale (SGS) combustion model to conduct the combustion process in a methane-air mixed gas pipeline containing double-seam obstacles. It was shown that the velocity of the flame front and the magnitude of the blast pressure during deflagration did not show a positive correlation with the size of the barrier slit spacing. They found that the flame front velocity of the obstacle with a slit spacing of 20 mm was maximum at 30 ms. The vorticity downstream of the obstacle gap was stronger when the obstacle gap spacing was 20 mm than when the obstacle gap spacing was 10 and 30 mm due to the presence of many intricate obstacles at the actual blast site and the inconsistent proximity of these obstacles to the source of the explosion.

Jiang et al. (2023) conducted research to investigate the effects of obstacle arrangement, obstacle proportion, and equivalence ratio on the detonation of hydrogen-air premixed gas. Their findings indicated that the spacing between obstacles and the obstruction ratio had significant impacts on parameters such as flame front speed, and blast pressure. In addition, a series of scholars have studied deflagration under propane–air premixed gases (Liu et al., 2015; Giurcan et al., 2020; Nakahara et al., 2021). Ruipengyu et al. (2021) used experiments to investigate the flame characteristics of stoichiometric propane–air premixed gases with obstacle perturbations and used the experimental results to verify the validity of the dynamic flame surface density (DFSD) model. Zhang et al. (2023) experimentally investigated the deflagration of propane–air premixed gases in square pipelines with large aspect ratios. The study revealed that a higher ratio of length to diameter of the pipeline, specifically at a ratio of 7, resulted in increased intensity of the reflected pressure wave effect within the pipe. This led to an acceleration in flame propagation speed and an increase in the frequency of overpressure oscillations. This study proved that turbulence did not destroy the internal structure of the flame but only changed the morphology. In addition, Gubba et al. (2011) performed experiments and LES calculations using a dynamic flame surface density (DFSD) model for a propane-air premixed gas explosion with a solid obstacle present. The positioning of the ignition source and solid obstacles were observed to have a notable impact on the flame structure and overpressure during deflagration.

According to the existing literature, the vast majority of studies selected a single type of obstacle. The placement of hurdle-type obstacles with square obstacles, a hybrid configuration, in pipelines for explosion studies has been relatively rare. Variations in the distance between an obstacle and the pipeline inlet can lead to changes in the effects of flame structure, explosion overpressure, and flow field characteristics during the deflagration process.

Therefore, this study utilized a combination of numerical simulations and experiments to examine the effects of a square obstacle arrangement with mixed obstacles on the deflagration characteristics of propane-air premixed gas in a semi-closed pipeline. The flame propagation and flow field characteristics of the square obstacle in the range of 250 to 850 mm from the ignition source were analyzed. This paper aimed to reveal the influence mechanism of the barrier perturbation on the deflagration process of propane–air premixed gases through a comparative analysis of the deflagration phenomena under different operating conditions. The key phenomena of the deflagration flow field were analyzed to reveal the relationships between the pressure peak, flame structure, and key parameters of the flow field and to investigate the effect of the mixed obstacle layout on the deflagration of propane–air premixed gases. The findings can guide the arrangement of equipment in confined and narrow spaces, offering significant guidance for the design of explosion-proof systems in such environments. The article aims to provide practical guidance on the avoidance and management of propane–air premixed gas explosions when assessing explosion risks.

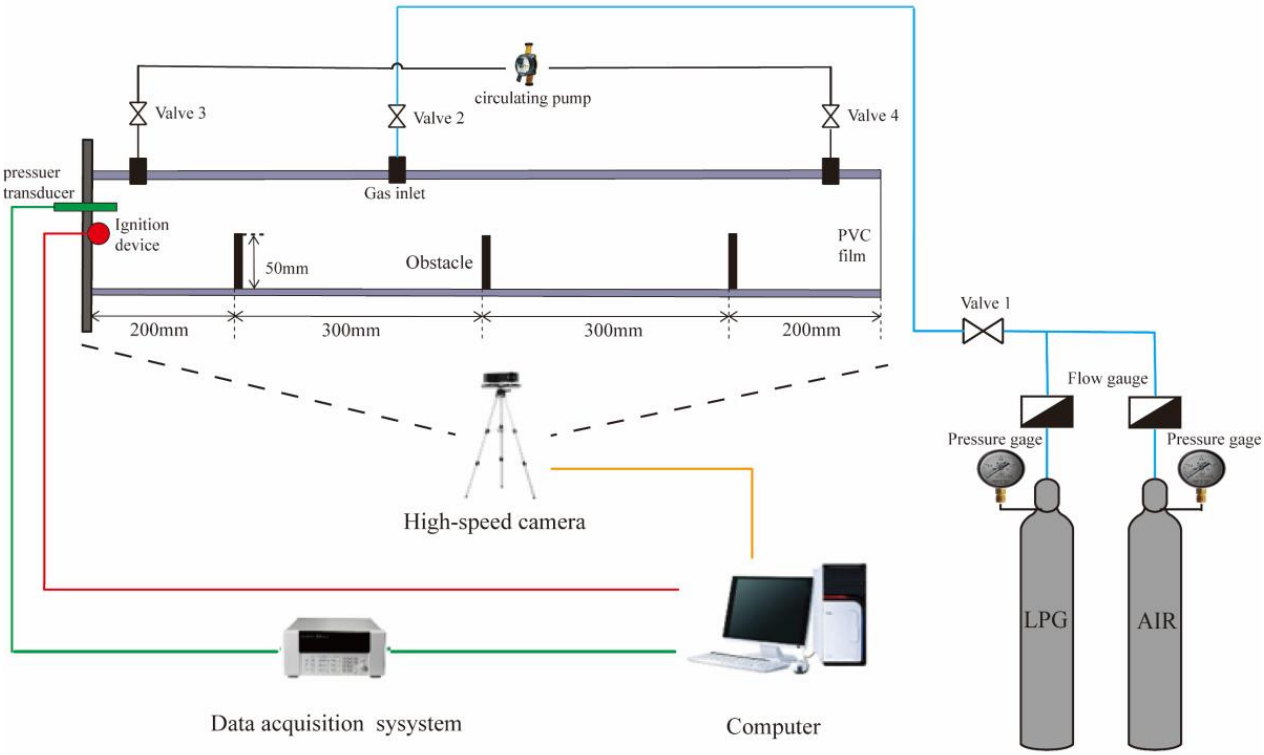

Fig. 1 Schematic diagram of the experimental system

2. EXPERIMENTAL SETUP AND METHODS

2.1 Experimental Setup

Figure 1 shows the piping arrangement. The dimensions of the whole visualization pipe were 100 mm × 100 mm × 1000 mm. The pipe was made of 5mm thick steel plates. To facilitate the capture of a clear image of the flame pattern, a Plexiglas plate that was 1000 mm long by 100 mm high by 20 mm wide was embedded in the right side of the pipe. The pipe mouth was sealed with a polyvinyl chloride (PVC) film to prevent fuel leakage. The top of the pipe was provided with an orifice for easy connection of the flexible tube.

In addition to this, several other devices were set up, all of which were connected to the computer for operation. The ignition system was a KTGD-B type, with an ignition frequency of 0.05 HZ and an electric spark energy of 0.5–20 J. The MC1362 camera had a resolution of 1280 × 1024 and a maximum frame rate of 500 fps. The CY400 pressure sensor sampling frequency was 200 kHz, with an error of ±0.25% and a range of 0–500 MPa. The accuracy of the data acquisition system was ±0.2%. The experiment was also set up with a J-LY-20 gas circulation pump, liquefied petroleum gas (LPG) cylinders, air cylinders, and valves. The maximum flow rate of the gas circulation pumps was 40 L/min and the maximum pressure was 25 kPa. The skin tube connected the LPG cylinder to the air cylinder. Control valve 1 delivered the gas mixture to the air inlet. The flow meter and pressure gauge were connected to the gas cylinder through the skin tube to control the filling of the gas. The propane–air mixture was delivered through the skin pipe to the air inlet into the duct after the speed was regulated by a 0.3 L/min flow meter. The pressure gauges, with input ranges and output ranges of 0–2.5 and 0–0.25 MPa, respectively, controlled the pressure of the LPG and air cylinders.

The holes at the top of the pipe near the inlet and outlet of the pipe were inserted into a skin tube to access the gas circulation pump so that the premixed gas was distributed more evenly throughout the chamber through circulation. Set up a high-speed camera right in the middle of the visual glass panel. Three flat barriers with dimensions of 100 mm × 50 mm × 5 mm were placed inside the tube 200, 500, and 800 mm from the ignition source. The entire experiment was conducted in a shaded environment to facilitate the capture of clear flame patterns.

2.2 Experimental Methods

First, flat barriers were fixed in the pipeline, and the computer, ignition system, high-speed camera, and data acquisition system were commissioned. Next, the pipe mouth was sealed with a plastic film to verify the airtightness of the entire pipe and prevent fuel leakage, the gas circulation pump was turned on, and valves 3 and 4 were opened at the same time to circulate the air in the pipe. Again, the LPG cylinder, air cylinder, and valve 1 were opened first, the gas was allowed to fill the skin tube, and then valve 2 was opened to control the LPG gas and the air charge through the flow meter and pressure gauge. The LPG air cylinder was closed after 90 s. Since there was previously reserved air inside the pipe after sealing the pipe with PVC film, the system was left open for 10 min, and then the air cylinder was closed. After the LPG and air were fully premixed and evenly distributed throughout the pipeline cavity by the gas circulation pump, all the valves and air bottles were closed. The LPG-to-air premix equivalent ratio of the entire chamber was 1.

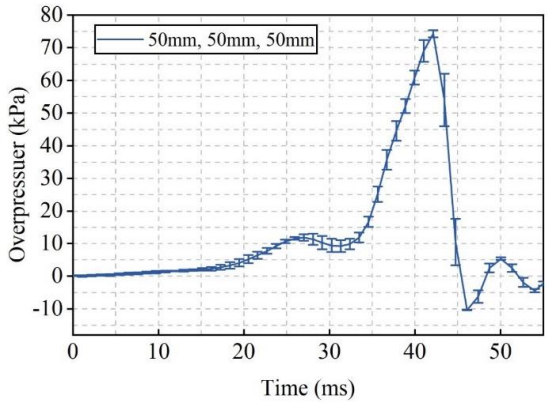

Fig. 2 Experimental overpressure curve over time under the condition of three flat obstacles with heights of 50 mm

Finally, the activation of the high-speed camera, data acquisition system, and ignition system was synchronized. The igniter was activated by a computer and has an ignition energy of 20 J. The experimental data were recorded by the data acquisition system. The detonation experiment was repeated at least three times at atmospheric pressure and an initial temperature of 300 K to ensure the accuracy of the data.

Figure 2 shows plots of the experimental overpressure versus time obtained by the above experimental method for three flat barriers with a height of 50 mm, a length of 100 mm, and a width of 5 mm.

3. NUMERICAL MODELS AND DETAILS

3.1 Governing Equations

In this study, the numerical simulations were mainly based on the LES method (Tartandyo et al., 2023; Wang et al., 2023b) implemented in the Fluent software, and the Zimont (Zimont & Battaglia, 2005) premixed combustion model was selected. The model equations were obtained by combining the fluid mass conservation equation based on Favre function filtration, the momentum conservation equation, and the energy conservation equation (Li et al., 2017; Xiu et al., 2023a). Using the Favre function as a filter, the LES governing equations were obtained as follows.

The mass conservation equation for the fluid flow is as follows:

$$\frac{\partial \rho}{\partial t}+\frac{\partial(\rho u_x)}{\partial x}+\frac{\partial(\rho u_y)}{\partial y}+\frac{\partial(\rho u_z)}{\partial z}=0 \tag{1}$$

where x, y, and z represent the three-dimensional rectangular coordinates, u_x, u_y, and u_z denote the fluid velocity components in the x-, y-, and z-directions, respectively, ρ denotes the density, and t denotes the time.

The momentum conservation of equations for the fluid flow is as follows:

$$\frac{\partial(\rho u_x)}{\partial t}+\nabla\cdot(\rho u_x\vec{\boldsymbol{u}})=-\frac{\partial p}{\partial x}+\frac{\partial T_{xx}}{\partial x}+\frac{\partial T_{yx}}{\partial y}+\frac{\partial T_{zx}}{\partial z}+\rho f_x \tag{2}$$

$$\frac{\partial(\rho u_y)}{\partial t}+\nabla\cdot(\rho u_y\vec{\boldsymbol{u}})=-\frac{\partial p}{\partial y}+\frac{\partial T_{xy}}{\partial x}+\frac{\partial T_{yy}}{\partial y}+\frac{\partial T_{zy}}{\partial z}+\rho f_y \tag{3}$$

$$\frac{\partial(\rho u_z)}{\partial t}+\nabla\cdot(\rho u_z\vec{\boldsymbol{u}})=-\frac{\partial p}{\partial z}+\frac{\partial T_{xz}}{\partial x}+\frac{\partial T_{yz}}{\partial y}+\frac{\partial T_{zz}}{\partial z}+\rho f_z \tag{4}$$

where f_x, f_y, and f_z represent the unit mass forces in the x-, y-, and z-directions, respectively, $\vec{\boldsymbol{u}}$ represents the velocity vector, p represents the pressure exerted on the fluid micrometric elements, and T_{xx}, T_{yx}, T_{zx}, T_{xy}, T_{yy}, T_{zy}, T_{xz}, T_{yz}, and T_{zz} represent the viscous stress components.

The energy conservation equation for the fluid flow is as follows:

$$\frac{\partial(\rho E)}{\partial t}+\nabla[\vec{\boldsymbol{u}}(\rho E+p)]=\nabla\cdot\left[k_{eff}\nabla T-\sum\nolimits_j h_j J_j+\tau_{eff}\vec{\boldsymbol{u}}\right]+S_h \tag{5}$$

where E represents the sum of the internal, kinetic, and potential energies of the fluid, k_{eff} represents the effective heat transfer coefficient, t_{eff} represents the viscous stress component, T represents the temperature, h_j represents the enthalpy, J_j represents the diffusive flux, $\vec{\boldsymbol{u}}$ represents the velocity vector, and S_h denotes the cumulative heat source term.

The c-equation for the LES method is obtained using the Favre function as a filter, as follows:

$$\frac{\partial(\bar{\rho}\tilde{c})}{\partial t}+\nabla\cdot(\bar{P}\tilde{u}\tilde{c})=\nabla\cdot\left(\frac{\mu_{eff}}{Sc_{eff}}\right)+\bar{S}_C \tag{6}$$

where ρ denotes the density, a horizontal line (-) above a symbol denotes a quantity filtered by the physical space filter, a wavy line (~) above a symbol denotes the amount filtered by the Favre filter, μ_{eff} denotes the effective viscosity, and S_C denotes the reaction source term.

3.2 Geometric Models and Initial Conditions

The schematic diagram of the physical model is shown in Fig 3(a). As shown in the figure, the entire numerical calculation domain was a square tube. The size is 100 × 100 × 1000 mm. The ignition source was set at the center of the pipe inlet. The entire pipe was semi-closed because it was not possible to construct the model with a PVC membrane at the pipe outlet, and the PVC membrane had a negligible effect on the state of the pipe. Three flat barriers with a blocking rate of 0.5 and a thickness of 5mm were arranged in the pipe and placed 200, 500, and 800 mm from the pipe's inlet, respectively.

To facilitate the numerical calculations, the experimental pipe geometry model was first constructed via computer-aided design software. Then, the established model was imported into the computational fluid dynamics (CFD) (Alibert et al., 2019; Momferatos et al., 2022; Olugbemide, 2022; Ustolin et al., 2022) software for mesh refinement. The mesh model is shown in Fig. 3(b). To ensure model validity, the overall quality of the delineated mesh was kept above 0.95. The whole computing domain was divided into a single grid of 3mm × 3mm, and the number of grids after division is 384948. Due to the short reaction time of the entire deflagration

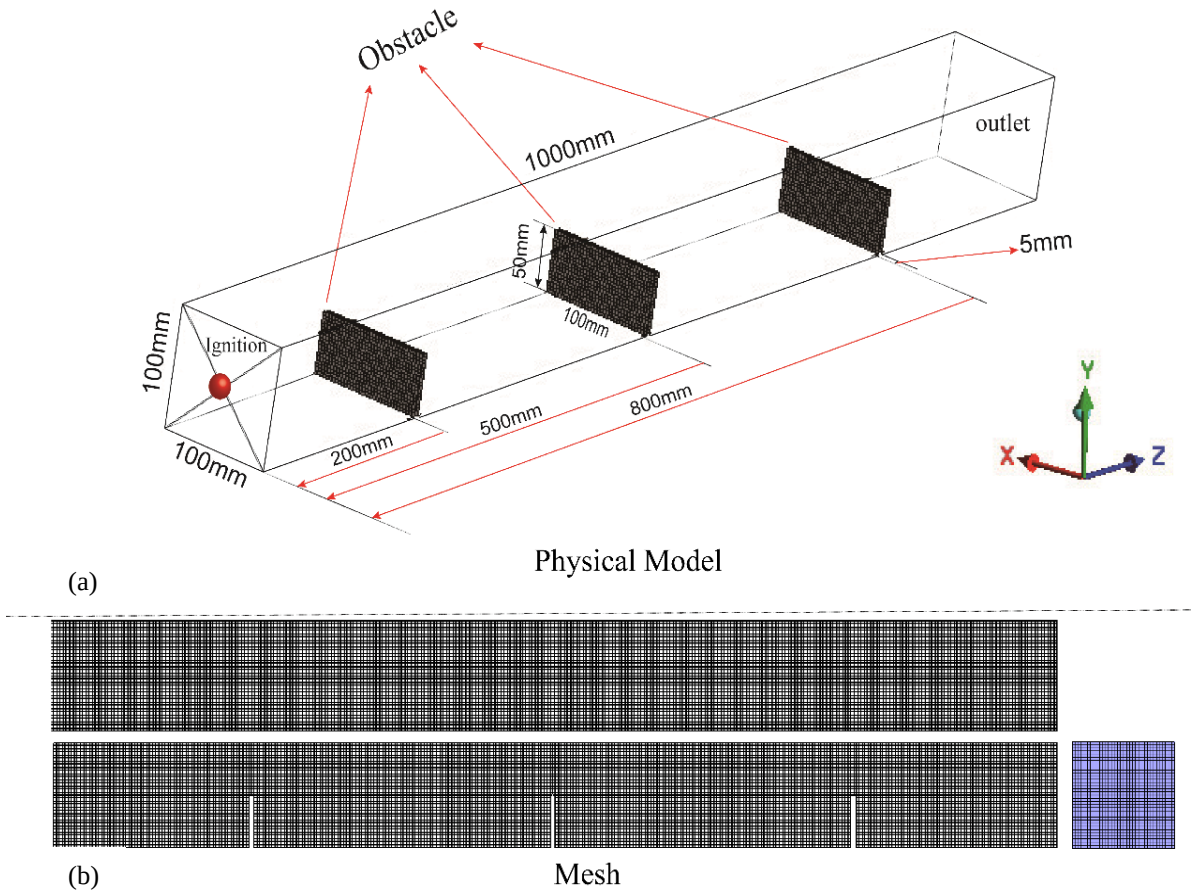

Fig. 3 Schematic diagrams of the geometric and grid models of the experimental setup

process, the reaction process of the flame and the wall surface of the pipe heat exchange was almost negligible.

Therefore, the pipe boundary conditions were set to non-slip and adiabatic walls. The boundary conditions at the pipe outlet were set to be reflection free to reduce the computational pressure and to avoid oscillatory attenuation of the pressure inside the pipe due to pressure waves. Before the calculation, the initial temperature of the pipe was set to 300 K, the reaction process variable was set to 0, and the initial pressure and initial flame speed were also set to 0. A hemispherical region with a diameter of 10 mm (Li et al., 2022a) was set at the center of the combustion chamber inlet, and its reaction process value was set to 1 to simulate ignition.

3.3 Numerical Details

98% of the components are propane for LPG. Therefore, based on the FLUENT software, the gas inside the entire combustion chamber was set to propane instead of LPG. Propane–air premixed gas under actual stoichiometric conditions is an ideal gas (Gao et al., 2022). The volume fraction of unburned propane fuel set in the platform was calculated to be 4.03% (chemical equivalent ratio of 1). The LES method has a high lattice resolution and the ability to simulate boundary layer turbulence in three dimensions. Thus, it is suitable for the study of various small- and medium-scale physical processes. Since the numerical model constructed for this study was also a small-scale pipeline model, we opted for large-vortex simulations.

Table 1 Model parameter settings

Parameter	Set value
Molecular weight (kg/kmol)	29.4652
Laminar flame speed (m/s)	0.36
Heat of combustion (J/kg)	5.0329×10^7
Thermal conductivity (W/(m K))	0.024
Unburnt fuel mass fraction	0.0603
Critical strain rate (s^{-1})	1×10^8

A series of studies have also shown that the LES method can better represent the validity of numerical simulations, so we selected the LES turbulence model (Li et al., 2022b; Pan et al., 2022; Ai et al., 2023; Jiang et al., 2024; Qiao et al., 2023). Combustion was simulated using the Zimont premix model. The specific heat capacities of unburned and burned mixtures were approximated by a segmented fifth-order polynomial function with respect to temperature, and the molecular viscosity was calculated by Sutherland's law (Hao et al., 2022). To ensure that the numerical calculations better fit the experiments, the values of specific parameters for the propane–air premixed gas combustion calculations are given in Table 1.

The time step in the numerical calculations was set to 3 × 10−6, and each time step was iterated 40 times to prevent calculation divergence (Hao et al., 2022). The residuals were below 1×10^{-6} for the energy equation, 1×10^{-3} for the process variable equation, and 1×10^{-5} for the other equations.

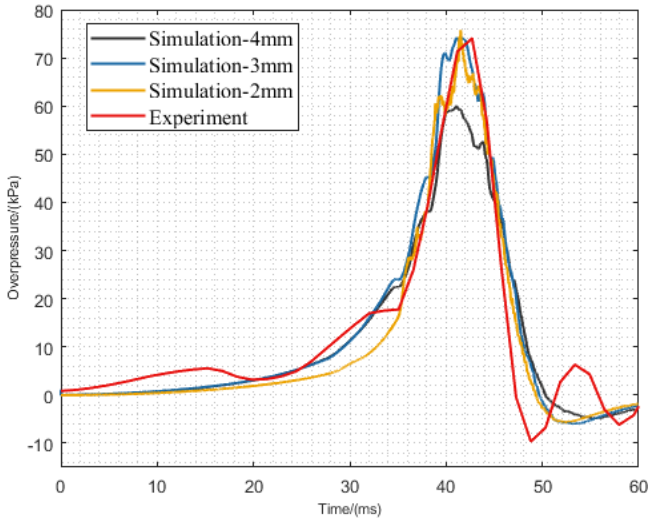

Fig. 4 Curves of simulated and experimental overpressure with time for different grid resolutions

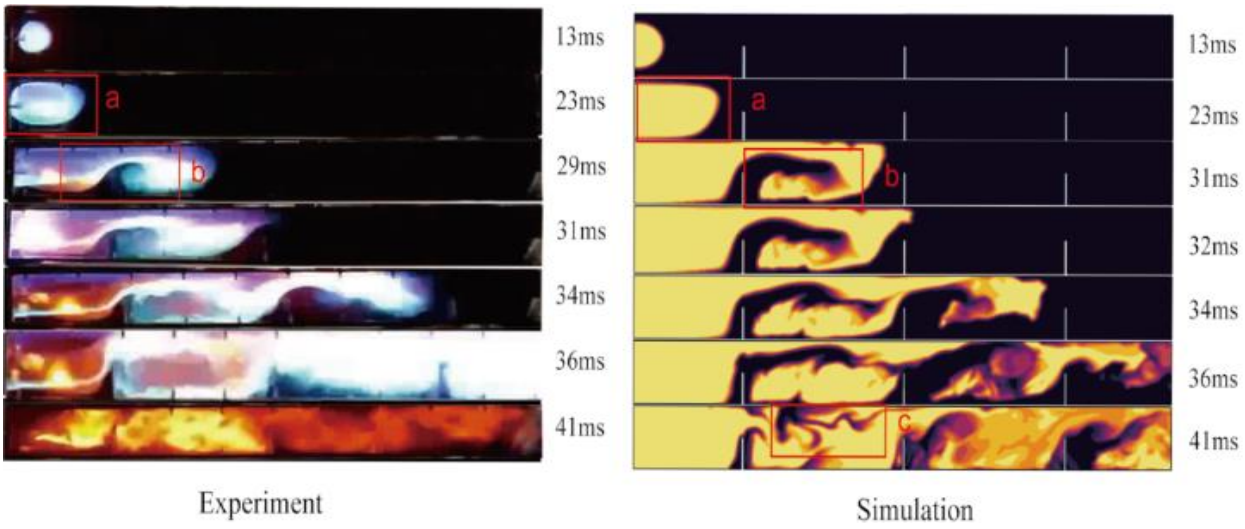

Fig. 5 Evolution of the flame propagation process with time in the experiment (left) and simulation (right)

4. RESULTS AND DISCUSSIONS

4.1 Model Verification

Figure 4 demonstrates the variation of the overpressure in the pipe over time throughout the deflagration process for different grid sizes. It is worth noting that when numerical simulations were performed with the three different mesh sizes and the rest of the parameter values were the same, the greater the mesh refinement, the better the simulation results fit the experiment. From the overall trend, the simulated overpressure curves at the remaining two grid sizes fit the experimental overpressure curves better than the simulated overpressure curves at the grid size of 4 mm × 4 mm. This was because the greater the mesh refinement was, the greater the number of mesh elements in the simulation was, the more complete the data needed for the simulation were, and the more accurate the calculation results were (Xiu et al., 2023a).

However, an increase in the number of grids significantly increases time costs and computing equipment requirements. Compared with the simulation with the 2 mm × 2 mm grid size, the simulation with the 3 mm × 3 mm grid size reduced the cost and time consumption while reproducing the amount of experimental data required. Clearly, the simulated overpressure curve with the 3 mm × 3 mm grid size fit well with the experimental overpressure curve. Considering the effectiveness of simulations and reduced computational costs, the final mesh size of 3 mm × 3 mm was selected in this study (Hao et al., 2022).

Figure 5 compares the flame structure of the experiment and simulation over time. Since the pipe was adiabatic under the simulated conditions and the actual pipe was not adiabatic, there was a temperature difference. Therefore, the flame propagation speed when conducting the experiment was in principle slightly faster than that in the simulation, but the difference was negligible. Clearly, the flame propagation pattern obtained from the simulated results was found to be highly consistent with the experimental. Considering the limitations of the frame rate of the shooting equipment used in the experiments and the

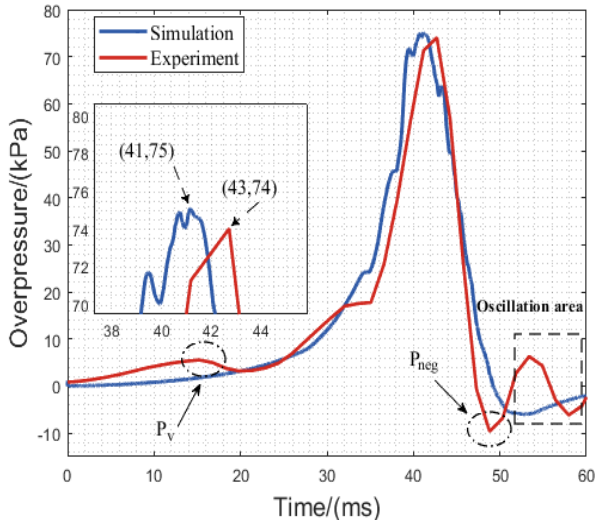

Fig. 6 Comparison of experimental and simulated overpressures over time

short duration of the entire flame deflagration process, some of the flame patterns in the experiments, especially details such as the flame deflagration, were difficult to capture.

Thus, the flame morphology details could be further examined through numerical simulations. At 13 ms, the flame morphology first propagated forward in a hemispherical shape (Li et al., 2017) and then transitioned to a finger-like shape, as illustrated in Fig 5's red box. The flame surface was smooth during this time period. The flame front passed the first flat obstacle at 29 ms, when the flame had been disturbed by the obstacle to become twisted and distorted, and the flame surface became wrinkled. The flame return state can be clearly seen in red box b in Fig. 5. It was obvious that during the period of 13-36 ms, under the stimulation of flat obstacles, the flame transitions from its initial smooth state to the state of the broken flame state, accompanied by a significant increase in flame propagation speed. Due to the disordered flame structure caused by the diffusion of unburned gas and deflagration in the combustion chamber, part of the fuel did not participate in the combustion reaction throughout the entire deflagration process. This resulted in the flame morphology having a special form, such as kite-type morphology, as illustrated in Fig 5's red box c. This suggested that numerical simulations were better able to show details of the flame morphology that could not be captured by the equipment. At 41 ms, the flame changed to an irregular flame cloud state due to the turbulence mechanism, and the whole combustion chamber flame was abnormally broken.

Figure 6 shows a comparison of the experimental and simulated overpressure profiles. The blue line is the simulated overpressure curve, and the red line is the experimental overpressure curve. Obviously, the simulated pressure results closely coincide with the experimental pressure results (Ai et al., 2023), which further confirmed that the numerical simulation was effective. The PVC film connected at the outlet of the pipeline was causing the peak in overpressure release.

Since the tube was in a closed state, the pressure in the tube rose for a short time after ignition, but the PVC film ruptured quickly to produce pressure relief (Li et al., 2021), and the overpressure dropped again. However, the simulation could not be set up with a pipe model with a PVC film at the outlet, and there was no PVC film rupture during the simulation. Therefore, the simulated curves did not produce peaks at the same moments. As shown in the figure, the simulated and experimental flames passed the first flat plate obstacle almost simultaneously at 29 ms. The overpressure curve thus increased rapidly. It is easy to see that the simulated overpressure peaked at 75 kPa at 41 ms and the experimental overpressure peaked at 74 kPa at 43 ms. This shows a relatively consistent value with a small error. The error between the maximum overpressures was calculated to be 1.35%. As the flame reached the outside of the pipe, the pressure inside the pipe drops sharply, and the overpressure curve dropped accordingly.

In addition, the pressure of unburned gas dropped rapidly after it flowed out of the pipeline, resulting in a pressure difference between the pipeline and the outside world. The peak negative overpressure is shown at P_{neg} of the experimental curve in Fig. 6. To maintain the balance of the unfired gas outside the tube backflowing into the tube, the overpressure inside the tube rose, which was the reason that P_{neg} was generated. The experimental overpressure curve produced oscillations, as shown by the black dashed box in the figure. This was because after the negative overpressure peak P_{neg} was created, the flame inside the tube burned and expanded again, pushing more unburned gas out of the tube. By repeating this, the amplitude of the pressure in the tube decreased during the cycle, and the oscillating pressure was gradually weakened (Fakandu et al., 2015), which is known as the Helmholtz resonator principle. The simulation curves did not oscillate because the orifice was set to be non-reflective, and the wall was adiabatic with no gas heat loss.

Both the comparison of the flame processes in the experimental and numerical simulations and the comparison of the overpressures in the experimental and numerical simulations further showed that the numerical simulations could reproduce the experimental process and results to a certain extent. Therefore, the correctness of the model was proven by this numerical validation, which provided the basis and conditions for the numerical simulation focused on later in this paper.

By comparing the flame structures as well as the overpressure curves at different moments of the experiment and simulation, it was found that the constructed model could reproduce the experimental data better. The error was also within manageable limits, further confirming the validity and goodness of the model. Therefore, on the basis of this model, the deflagration characteristics of the propane–air premixed gases were investigated in this mixing configuration of hurdle-type and square obstacles. Figure 7 shows the four different configurations studied in this paper, and for comparison purposes, the first set of configurations was set with three hurdle-type obstacles, which did not include square obstacles.

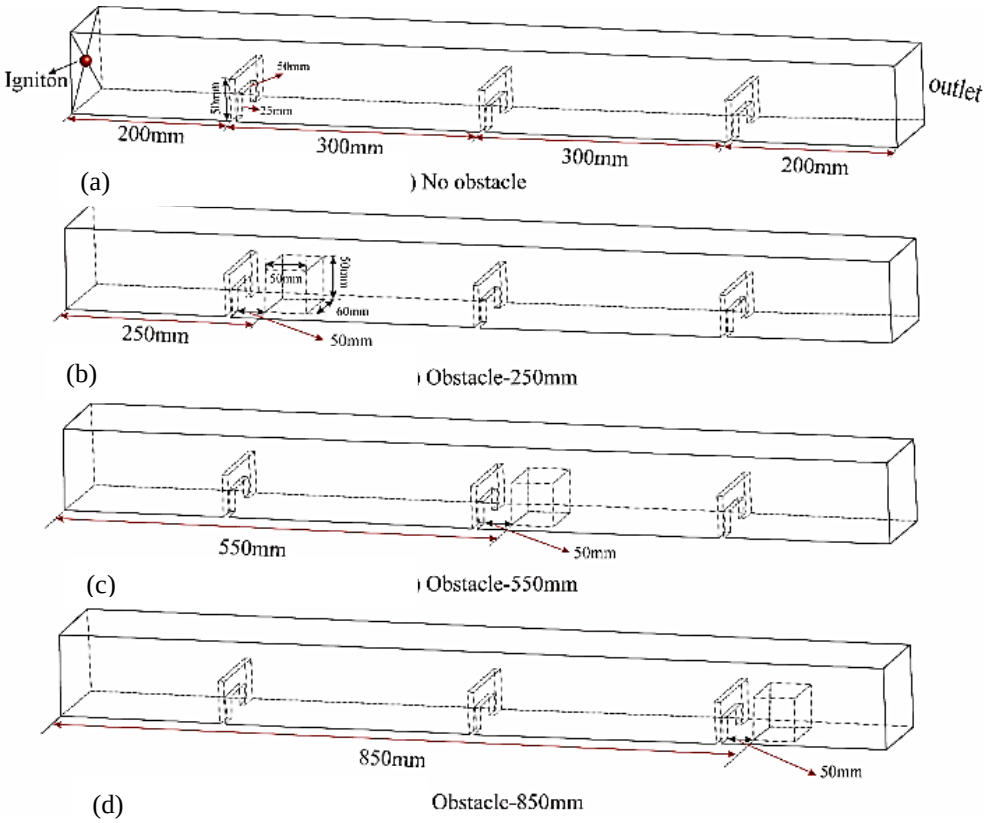

Fig. 7 Three-dimensional structural diagrams in four configurations

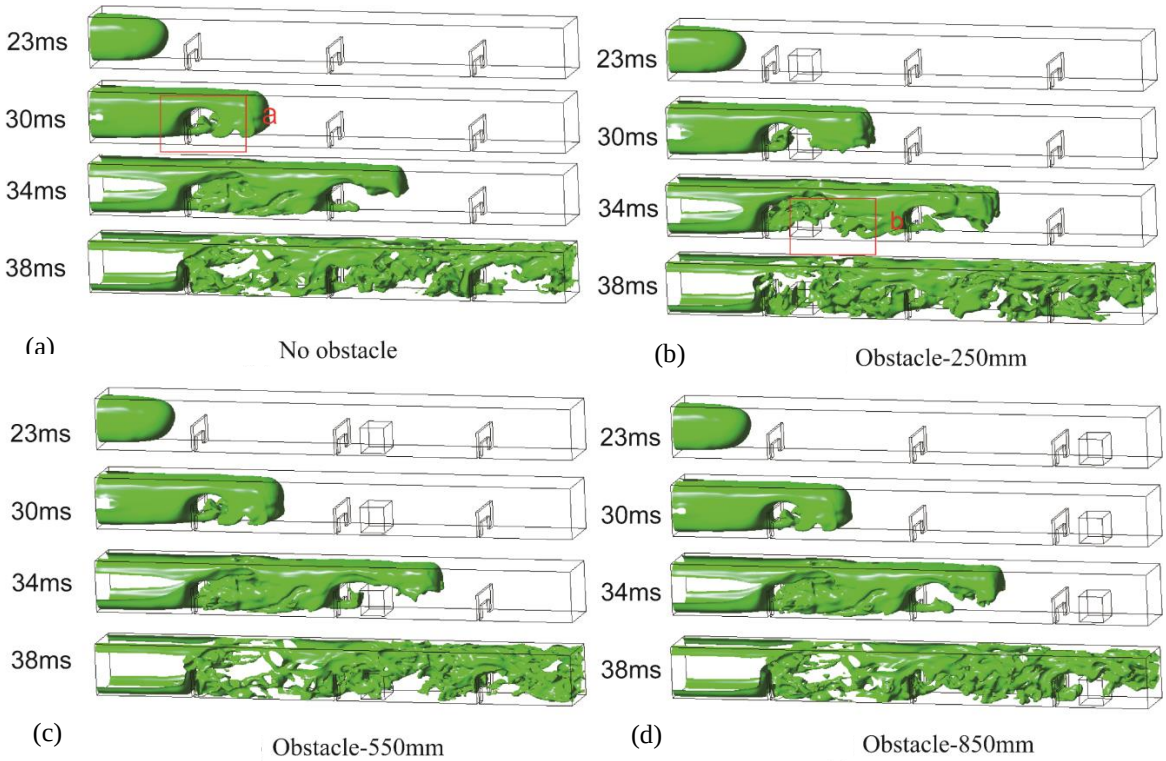

Fig. 8 Schematic of the evolution of the three-dimensional premixed flame structure over time

4.2 Flame Propagation Patterns and Processes

Figure 8 shows the evolution of the three-dimensional premixed flame structure over time for different square obstacle layouts. To facilitate the observation of the flame structure, an isosurface with the reaction process variable c = 0.5 was selected to simulate the flame front propagation process in this study (Xu, 2015). Clearly, the flame propagation in all four configurations at 23 ms was in the early stage and had not been disturbed by the first hurdle-type obstacle, the flame surface was wrinkle-free and smooth, and the flame structure propagated forward in a finger-like shape. It is easy to see that the flame

structures that were unperturbed by obstacles at 23 ms were approximately the same for the four configurations. At this time, the flame structure was relatively smooth, and the flame propagation speed and flame surface area did not show significant changes.

At 30 ms, the flame began to contact the first hurdle-type obstacle, the flame structure began to twist, and the flame surface area increased to propagate faster. At the same time, the flame rushed out from the pipe wall and the upper end of the obstacle, as well as the opening position under the obstacle, forming a flame structure that spread forward in a cat's paw shape. Owing to the turbulent flow of flame in the entire combustion chamber during the deflagration process, the flame front formed a reflux area and gradually converged to the flame at the tube wall when it passed through the opening under the hurdle-type obstacle, as illustrated in Fig 8's red box.

Further, in Fig. 8(b), at 30 ms, the flame was excited by the square obstacle, and it spread farther, and the distortion of the flame surface was more evident than in the remaining three configurations. It was further shown that the mixed obstacles promoted flame development more than single obstacles at the same moment. At 34 ms, it is remarkable that the flame propagation velocity was enhanced in all four configurations, because all the flames were excited by the first hurdle-type obstacle. Compared with the remaining three configurations at that moment, the flame front of this configuration in Fig. 8(c) reached farther away. Figure 8(b) shows a thin flame reaction zone at the right rear end of the square obstacle at 34 ms. This was due to obstructions interfering with the flame structure during the initial phases of the deflagration process. The flame surface area then began to increase, which caused the unburned gas body in the tube that was at the front of the flame to be squeezed into the back end of the square obstacle to form a vacancy (Li et al., 2017), as shown in red box b in Fig. 8(b).

After 38 ms, the deflagration of the four configurations was about to end, and the flame patterns in the combustion chamber were abnormally fragmented. Furthermore, at 38 ms, the flame in this configuration in Fig. 8(d) did not show increases in the flame surface area and the distance the flame travels forward because it passed through the square obstacle. This was because the square obstacle in Fig 8(b) was positioned too far back. When the flame reached this position, it was subjected to the pressure wave action of the tube wall and the obstacle, which accelerates the leakage out of the tube, and the flame turbulence inside the pipe was greatly reduced. As a result, the flame surface area and flame propagation speed did not change significantly. In summary, when the square obstacle was at a critical distance from the ignition source position, the mixed obstacle had a positive feedback effect on flame excitation.

4.3 Effect of Layout on Explosive Overpressure

Figure 9 illustrates the overpressure curve over time for the four configurations. In general, the curves of the four configurations showed a trend of initially increasing, then decreasing, and finally stabilizing (Bychkov et al., 2007; Nguyen et al., 2021; Zheng et al., 2023). Clearly,

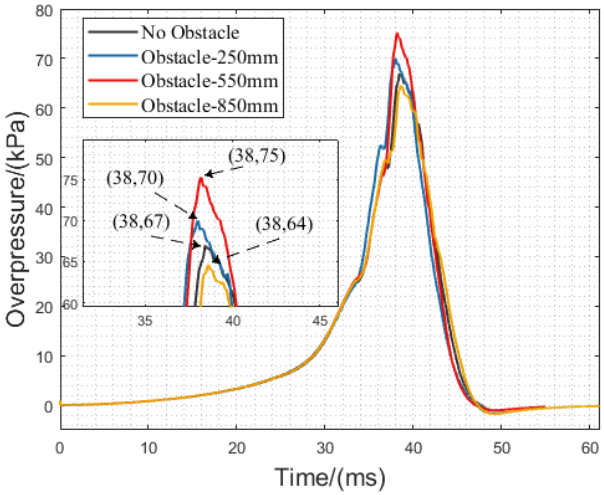

Fig. 9 Comparison of overpressure variations with time for different configurations

the overpressures of the four configurations increased rapidly at about 26 ms. This was because the flame patterns in the four configurations were almost identical at the beginning of the flame propagation, and the flames were all simultaneously excited by the first hurdle-type obstacle.

Thus, the four configurations showed consistent increases in the overpressure at 26 ms. It is clearly seen that the #Obstacle-550 mm configuration had the largest overpressure of 75 kPa at about 38 ms. This was because this configuration had more ample space to promote flame development and heat buildup relative to the #Obstacle-250 mm configuration, which further incentivized an increase in the overpressure. This was because when the flame propagates forward, it was stimulated by the square obstacle, which intensified the flame evolution and accelerated the flame propagation.

However, the overpressure was compromised by the fact that the flame was about to burst out of the pipe, creating pressure relief. Therefore, the #Obstacle-850 mm configuration had the lowest peak overpressure. Since the flames in the #No obstacle configuration were not stimulated by the square obstacle, neither the flame propagation rate nor the explosion overpressure was as large as those for the #Obstacle-250 mm and #Obstacle-550 mm configurations. Again, due to the lack of square obstructions in the pipe, flame propagation did not result in excessive pressure relief due to the flame being promoted to rush out of the pipe as in the #Obstacle-850 mm configuration. Thus, the #No obstacle configuration had the third-highest peak overpressure.

Figure 9 shows that at 38 ms, the overpressure is 75 kPa for the #Obstacle-550 mm configuration, 70 kPa for the #Obstacle-250 mm configuration, 67 kPa for the #No Obstacle configuration, and 64 kPa for the #Obstacle-850 mm configuration. Of these, the overpressure for #Obstacle-850 mm was 17.19% greater than that for #Obstacle-550 mm. By contrast, the overpressure for #Obstacle-850 mm was 9.38% greater than that for #Obstacle-250 mm, and it was 4.69% greater than that for #No Obstacle. This indicated that at the square obstacle

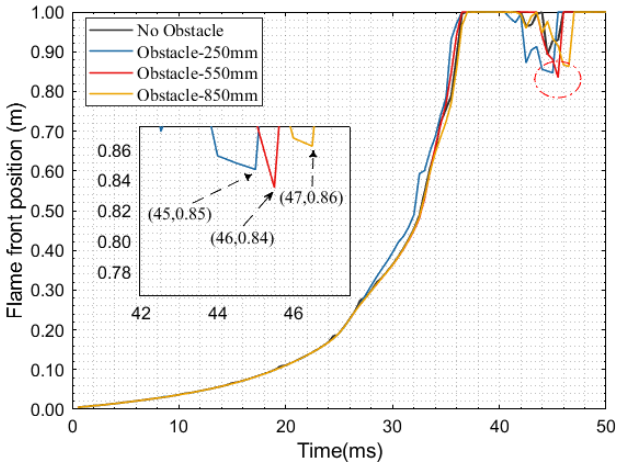

Fig. 10 Comparison of flame front position variations with time for different configurations

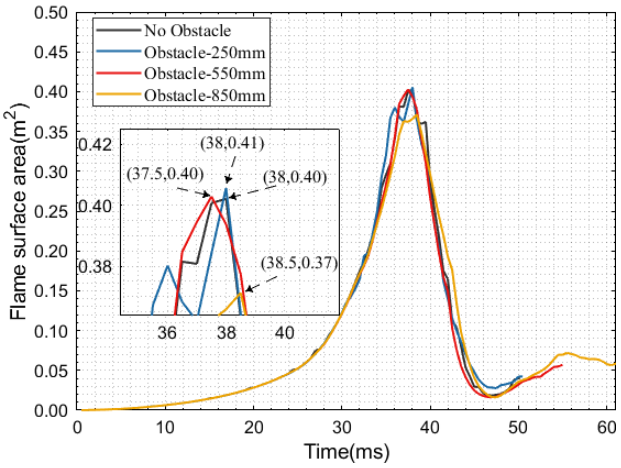

Fig. 11 Comparison of flame surface area variations with time for different configurations

furthest from the ignition source, the flame elongated along the flow direction as it passed through the channel between the obstacle and the pipe wall, which was mainly due to the violent flow field contraction and the pressure wave. This instability created a shear layer on the left and right flame surfaces and formed small vortices. The maximum overpressure resulting from the further acceleration of the flame out of the pipe was the lowest of the four sets of conditions.

4.4 Impact of Layout Style on Flame Front Position

Figure 10 illustrates a comparison of the flame front position over time under four different conditions. After 26 ms, the #Obstacle-250 mm configuration had a faster flame propagation rate than the rest of the configurations. For the same amount of time, the #Obstacle-250 mm configuration flame front traveled further than those of the other configurations. In this configuration, the flame was initially excited by the square obstacle, and the number of folds on the flame surface increased.

This resulted in the presence of square obstacles that constrict the flame, leading to the compression of the flame structure and causing it to travel faster. Similarly, at 34 ms, flame propagation was accelerated in the #Obstacle-550 mm configuration. As shown in the figure, since the #Obstacle-250 mm configuration was the first to be excited by the square obstacle, resulting in the fastest flame propagation, it was the first to rush out of the pipe. Therefore, it was also the first to produce a flame backflow. The reason for the flame backflow was that the premixed flame burns in the pipeline, causing a sudden rise in pressure in the combustion chamber. In order to balance the internal and external pressure in the combustion chamber, the flame produced a backflow phenomenon. The red dashed ellipse portion of the graph shows that the #Obstacle-550 mm configuration produced the most pronounced backflow from the flame.

In conclusion, there was a coupling relationship between the flame propagation velocity, explosion overpressure, and flame surface area. Figure 9 shows that the #Obstacle-550 mm configuration had a higher peak overpressure than the other configurations. Therefore, to balance the pressure inside and outside the combustion chamber throughout the deflagration process, the flame backflow in the # Obstruction-550 mm configuration is more pronounced than in other configurations.

4.5 Influence of Layout Style on Flame Area

Figure 11 demonstrates the curve of the flame surface area over time for the four configurations. It can be observed that the curve trends for the four configurations in the figure. They first increased, then decreased, and then exhibited a small increase. The flame in the #Obstacle - 250 mm configuration rapidly increased its surface area upon first contact with the square obstacle. This was due to the contact with a square obstacle, where the flame front squeezed against the obstacle, creasing the flame surface and increasing the flame surface area. The flame surface area peaked at 38 ms for all four configurations. At this point, the deflagration process was nearing completion, and the combustion chamber was filled with flames. Thus, the flame surface area in all four configurations peaked at this moment.

Upon completion of the deflagration process, the flame extended outside the pipe, resulting in a reduced flame surface area. As a result, the graph showed a trend of peaking and then declining. At 40–44 ms, the #Obstacle-850 mm configuration had a larger flame surface area than the other configurations. Because the square obstacle in the # obstacle-850mm configuration was positioned too far back, a significant amount of fuel was left at the pipeline exit. At the same time, under the excitation of the square obstacle, a large amount of fuel was squeezed out of the tube by the flame, and the flame continues to burn outside the pipe, further increasing the surface area of the flame. In the remaining configurations, most of the fuel remained in the combustion chamber, with only a small amount escaping with the flame through the pipe. In contrast, the flame surface area curve of #Obstacle-850mm for this configuration was more distinctive than for the other configurations.

Based on the comparison of the four sets of conditions, the largest and smallest flame front areas were 0.41 and 0.37 m^2, respectively. The flame front area of

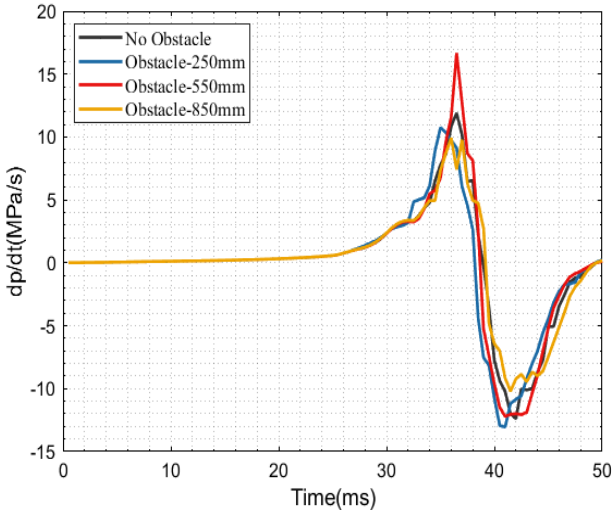

Fig. 12 Comparison of overpressure rise rate variations with time for different configurations

#Obstacle-850 mm increased by 10.81% compared with that of #Obstacle-250 mm. Compared to #Obstacle-550 mm, #Obstacle-850 mm exhibited a 2.5% increase in flame front area, while compared to #No Obstacle, #Obstacle-850 mm had a 2.5% larger flame front area. For the #Obstcle-250 mm configuration, the flame front area was the largest because the flame first passed the hurdle obstacle and then passed the square obstacle during the initial deflagration process. Due to the turbulence mechanism, the flame inside the pipe was disturbed to form an irregular flame cloud pattern. The flame changed from a banded flame to an irregular flame cloud that spread over the pipe lumen, therefore, the flame front area expanded.

4.6 Influence of Layout on Rise Rate of Overpressure

Figure 12 shows the curve of pressure rise rate over time for the four configurations. The rate of overpressure rise can also be used to reflect the intensity of the explosion and the rate of flame burning (Xiu et al., 2023a). At 0-30 ms, the trend curves of the four configurations in the figure are essentially identical. The reason is at the beginning of the deflagration process, the flames in all four configurations did not contact the square obstacles as they propagated forward, so the trend of the curve is almost the same.

The rate of overpressure rise for the #Obstacle-250 mm configuration was the first to increase significantly at about 32 ms. The obstacle triggered the development of the flame, causing a rapid increase in overpressure within the pipeline. As a result, the overpressure rise rate curve for the #Obstacle-250 mm configuration was more pronounced in the time period of 32–36 ms than those of the other configurations. As can be seen in the figure, the #Obstacle-550 mm configuration had the largest peak overpressure rise rate at 38 ms, which was also the largest explosion intensity. As the distance of the square obstacle from the pipe inlet location increased, whether the position of the square obstacle was at the appropriate critical value affected the speed of overpressure rise.

4.7 Relationship Between Flame Propagation Process, Maximum Pressure and Eddy Current

Figure 13 demonstrate the flow field over time after ignition of the premixed gas. The black curve depicts the flame structure, the white wavy line represents the velocity streamline, and the colored background map represents the pressure distribution map during deflagration. At 30 ms, it can be seen that the streamlines near the square obstacle in Fig. 13(b) were extremely dense and a clockwise-rotating vortex was generated at the left end of the square obstacle. The flame propagated forward but was interfered with by the first hurdle obstacle, causing the flame to be squeezed downward and disturbing the nearby flow field. This squeezes the unburnt gas at the flame front, causing the gas to be squeezed between the hurdle obstacle and the square obstacle, which in turn creates a turbulent vortex.

As illustrated in Fig 13's blue box, no turbulent vortices were generated near the first hurdle-type obstacle for the remaining three configurations at the same moment. It can be seen that this combined configuration of hurdle-type obstacles and square obstacles promoted vortex formation. At 34 ms, #Obstacle-250mm flame propagation was the fastest among the four configurations. This was because the presence of vortices promoted flame development, enhanced the flame burning rate. Further from the pressure contour plot, the maximum overpressure of the #Obstacle-550 mm configuration was about 75 kPa at 38 ms. Next, the maximum overpressures for the #Obstcale-250 mm, #No obstacle, and #Obstacle-850 mm configurations were 70, 67, and 64 kPa. Furthermore, vortices appeared near the square obstacle in the #Obstacle-550 mm configuration, as shown at the red box in the figure. The presence of the vortex broke up the entire flame structure and the previously banded flame became fragmented. It is evident that the #Obstacle-850 mm configuration did not produce strong vorticity in the vicinity of the square obstacle. It was further shown that the hybrid obstacle promoted vortex generation more when the square obstacle was at a critical distance from the ignition source location.

5. CONCLUSIONS

In this study, experiments were combined with numerical simulations to investigate the effect of the layout of square obstacles in configurations with mixed obstacle types on the deflagration characteristics of propane–air premixed gases. Then, the structure of the flow field during deflagration was further analyzed. The conclusion is as follows:

(1) At the same moment, the two configurations of #Obstacle-250mm and #Obstacle-550mm promoted the generation of flame surface folds, increased the flame area, and increased the flame propagation speed more than configurations without square obstacles. At 30 ms, the flame in the four configurations formed a cat's paw pattern near the thin reaction zone of the combustion chamber.

(2) Among the four configurations, the #Obstacle-550 mm configuration had the highest peak overpressure, the maximum overpressure rise rate peaks, and the most

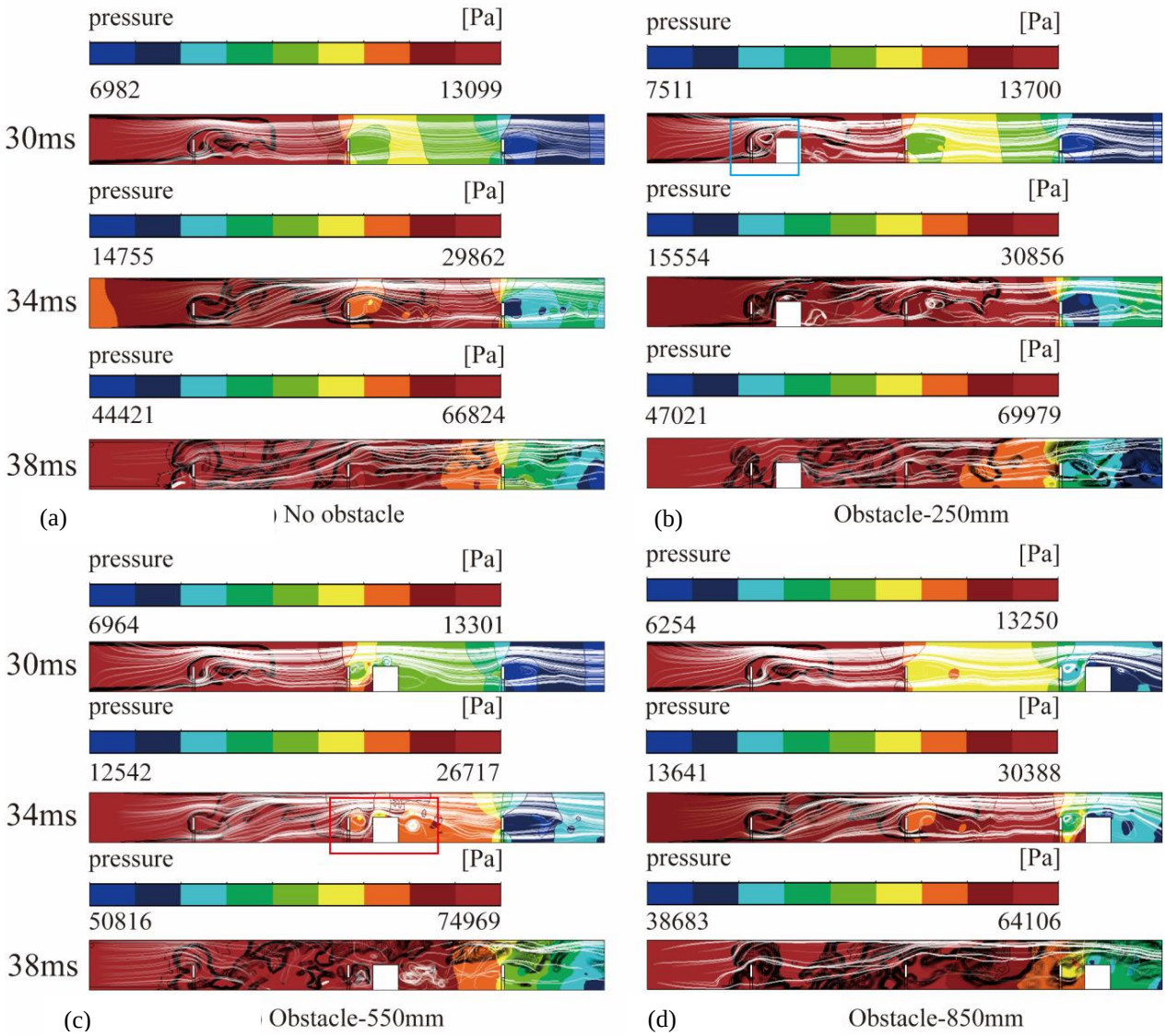

Fig. 13 Explosion overpressure, velocity, and flame structure with time for different configurations

pronounced reflux effect when the flames reached the outside of the pipe. Furthermore, the maximum pressure, flame surface area, flame front position, and overpressure rise rate were all maximized at the same moment in all four configurations at 38 ms.

(3) In the case of mixed obstacles, when the square obstacle's position away from the pipe inlet was within a certain critical value, there was a more obvious effect on the flame excitation, but beyond the critical value, flame development was inhibited. However, due to laboratory equipment limitations, accurate critical values could not be measured at this time. In future research, we will further investigate this critical value to arrive at an exact value.

(4) Mixed obstacles contributed to vortex generation, but there was also a special phenomenon generated by the #Obstacle-850 mm configuration. The square obstacle was too close to the exit, allowing the flame to rush out of the pipe prematurely, inhibiting vortex generation. The square obstacle distance from the ignition source was in a transition from a 250 mm distribution to a 550 mm distribution, where the further the square obstacle position was from the ignition source, the stronger the vortex in the flow field became. To further illustrate this, when the distance between the square obstacle and the pipe inlet was in the range of 250–550 mm, the distance was linearly correlated with the strength of the vortices in the flow field.

Future research will further explore the exact critical value of the distance from the ignition source location for square obstacles with strong flame excitation in mixed obstacle layouts. The results can offer practical guidance for the layout of large enclosed space facilities and equipment. In the future, we will also study the deflagration of premixed flammable gases, such as hydrogen-doped natural gas, in a confined space.

ACKNOWLEDGEMENTS

This research was funded by the basic public welfare research project of Zhejiang the province, grant number LGF22E040002.

We thank LetPub (www.letpub.com) for its linguistic assistance during the preparation of this manuscript.

CONFLICT OF INTEREST

The authors declare that they have no known competing financial interests or personal relationships that could have appeared to influence the work reported in this paper.

AUTHORS CONTRIBUTION

Yang Wu developed the numerical model, conducted the simulations, wrote the manuscript, and prepared all the figures. **Jianfeng Gao** supervised and guided the work with his advice due to his considerable experience in this field. Finally, **Yanan Han, Bingjian Ai**, **Xiaojun Shao**, **Bingang Guo,** and **Bin Hao** reviewed and revised the manuscript before submission.

REFERENCES

Ai, B., Gao, J., Hao, B., Guo, B., & Liang, J. (2023). Effect of obstacle length variation on hydrogen deflagration in a confined space based on large eddy simulations. *Journal of Applied Fluid Mechanics*, *17*(2), 384-397. https://doi.org/10.47176/jafm.17.02.2106

Alibert, D., Coutin, M., Mense, M., Pizzo, Y., & Porterie, B. (2019). Effect of oxygen on the burning behavior of liquid and solid fuels in a large-scale calorimeter. *Journal of Applied Fluid Mechanics*, *12*, 37-47. https://doi.org/10.36884/jafm.12.SI.29932

Baraza, X., Cugueró-Escofet, N., & Rodríguez-Elizalde, R. (2023). Statistical analysis of the severity of occupational accidents in the mining sector. *Journal of Safety Research*, *86*, 364-375. https://doi.org/https://doi.org/10.1016/j.jsr.2023.07.015

Bo, Y., Li, Y., & Gao, W. (2023). Exploring the effects of turbulent field on propagation behaviors in confined hydrogen-air explosion using OpenFOAM. *International Journal of Hydrogen Energy*. https://doi.org/https://doi.org/10.1016/j.ijhydene.2023.07.303

Bychkov, V., Akkerman, V. Y., Fru, G., Petchenko, A., & Eriksson, L. E. (2007). Flame acceleration in the early stages of burning in tubes. *Combustion and Flame*, *150*(4), 263-276. https://doi.org/https://doi.org/10.1016/j.combustflame.2007.01.004

Cao, W., Zhou, Z., Zhou, W., Xu, S., Xiao, Q., Cao, W., Jiao, F., Zhang, Y., Yu, S., & Xu, S. (2022). The flow field behaviours of under-expansion jet flame in premixed hydrogen/air explosion venting. *International Journal of Hydrogen Energy*, *47*(18), 10420-10430. https://doi.org/https://doi.org/10.1016/j.ijhydene.2022.01.082

Chen, P., Sun, Y., Li, Y., & Luo, G. (2017). Experimental and LES investigation of premixed methane/air flame propagating in an obstructed chamber with two slits. *Journal of Loss Prevention in the Process Industries*, *49*, 711-721. https://doi.org/https://doi.org/10.1016/j.jlp.2016.11.005

Cheng, F., Chang, Z., Luo, Z., Liu, C., Wang, T., & He, C. (2020). Large eddy simulation and experimental study of the effect of wire mesh on flame behaviours of methane/air explosions in a semi-confined pipe. *Journal of Loss Prevention in the Process Industries*, *68*, 104258. https://doi.org/https://doi.org/10.1016/j.jlp.2020.104258

Ciccarelli, G., Chaumeix, N., Mendiburu, A. Z., N'Guessan, K., & Comandini, A. (2019). Fast-flame limit for hydrogen/methane-air mixtures. *Proceedings of the Combustion Institute*, *37*(3), 3661-3668. https://doi.org/https://doi.org/10.1016/j.proci.2018.06.045

Fakandu, B. M., Andrews, G. E., & Phylaktou, H. N. (2015). Vent burst pressure effects on vented gas explosion reduced pressure. *Journal of Loss Prevention in the Process Industries*, *36*, 429-438. https://doi.org/https://doi.org/10.1016/j.jlp.2015.02.005

Gao, J. F., Ai, B. J., Hao, B., Guo, B. G., Hong, B. Y., & Jiang, X. S. (2022). Effect of obstacles gradient arrangement on non-uniformly distributed LPG-air premixed gas deflagration. *Energies*, *15*(19), 6872. https://doi.org/10.3390/en15196872

Giurcan, V., Mitu, M., Movileanu, C., Razus, D., & Oancea, D. (2020). Influence of inert additives on small-scale closed vessel explosions of propane-air mixtures. *Fire Safety Journal*, *111*, 102939. https://doi.org/https://doi.org/10.1016/j.firesaf.2019.102939

Goodwin, G. B., Houim, R. W., & Oran, E. S. (2016). Effect of decreasing blockage ratio on DDT in small channels with obstacles. *Combustion and Flame*, *173*, 16-26. https://doi.org/https://doi.org/10.1016/j.combustflame.2016.07.029

Gubba, S. R., Ibrahim, S. S., Malalasekera, W., & Masri, A. R. (2011). Measurements and LES calculations of turbulent premixed flame propagation past repeated obstacles. *Combustion and Flame*, *158*(12), 2465-2481. https://doi.org/https://doi.org/10.1016/j.combustflame.2011.05.008

Han, S., Yu, M., Yang, X., & Wang, X. (2020). Effects of obstacle position and hydrogen volume fraction on premixed syngas-air flame acceleration. *International Journal of Hydrogen Energy*, *45*(53), 29518-29532. https://doi.org/https://doi.org/10.1016/j.ijhydene.2020.07.189

Hao, B., Gao, J. F., Guo, B. G., Ai, B. J., Hong, B. Y., & Jiang, X. S. (2022). Numerical simulation of premixed methane-air explosion in a closed tube with U-type obstacles. *Energies*, *15*(13), 4909. https://doi.org/10.3390/en15134909

He, Z., Wu, Q., Wen, L., & Fu, G. (2019). A process mining approach to improve emergency rescue processes of fatal gas explosion accidents in Chinese coal mines. *Safety Science*, *111*, 154-166. https://doi.org/https://doi.org/10.1016/j.ssci.2018.07.006

Ismail, S., Ramli, A., & Abdul Aziz, H. (2021). Research trends in mining accidents study: A systematic literature review. *Safety Science*, *143*, 105438. https://doi.org/https://doi.org/10.1016/j.ssci.2021.105438

Jiang, Y., Gao, W., Sun, Z., Liang, B., Zhang, K., & Li, Y. (2023). Experimental and numerical study on explosion behavior of hydrogen-air mixture in an obstructed closed chamber. *International Journal of Hydrogen Energy*. https://doi.org/https://doi.org/10.1016/j.ijhydene.2023.08.159

Jiang, Y., Qiu, S., Gao, W., Liang, B., & Li, Y. (2024). Hydrogen flame acceleration and explosion overpressure characteristics in a closed obstructed duct. *International Journal of Hydrogen Energy*, *59*, 1-9. https://doi.org/https://doi.org/10.1016/j.ijhydene.2024.01.291

Kagan, L., & Sivashinsky, G. (2023). Effect of the central gravitational field on self-accelerating outward propagating flames subjected to the Rayleigh-Taylor instability: Transition to detonation. *Combustion and Flame*, *256*, 112951. https://doi.org/https://doi.org/10.1016/j.combustflame.2023.112951

Kindracki, J., Kobiera, A., Rarata, G., & Wolanski, P. (2007). Influence of ignition position and obstacles on explosion development in methane–air mixture in closed vessels. *Journal of Loss Prevention in the Process Industries*, *20*(4), 551-561. https://doi.org/https://doi.org/10.1016/j.jlp.2007.05.010

Korytchenko, K., Senderowski, C., Samoilenko, D., Poklonskiy, E., Varshamova, I., & Maksymov, A. (2022). Numerical analysis of the spark channel expansion in a high-pressure hydrogen-oxygen mixture and in nitrogen. *Shock Waves*, *32*(4), 321-335. https://doi.org/10.1007/s00193-022-01077-3

Li, Du, Y., Wang, S., Qi, S., Zhang, P., & Chen, W. (2017). Large eddy simulation and experimental study on vented gasoline-air mixture explosions in a semi-confined obstructed pipe. *Journal of Hazardous Materials*, *339*, 131-142. https://doi.org/https://doi.org/10.1016/j.jhazmat.2017.06.018

Li, Wu, J., Wang, S., Bai, J., Wu, D., & Qi, S. (2021a). Effects of gas concentration and obstacle location on overpressure and flame propagation characteristics of hydrocarbon fuel-air explosion in a semi-confined pipe. *Fuel*, *285*, 119268. https://doi.org/https://doi.org/10.1016/j.fuel.2020.119268

Li, R., Luo, Z., Cheng, F., Wang, T., Lin, H., & Liu, H. (2021b). A comparative investigation of premixed flame propagating of combustible gases-methane mixtures across an obstructed closed tube. *Fuel*, *289*, 119766. https://doi.org/https://doi.org/10.1016/j.fuel.2020.119766

Li, G., Zheng, K., Wang, S., & Chen, W. (2022a). Comparative study on explosion characteristics of hydrogen and gasoline vapor in a semi-confined pipe based on Large Eddy Simulation. *Fuel*, *328*, 125334. https://doi.org/https://doi.org/10.1016/j.fuel.2022.125334

Li, G., Zheng, K., Wang, S., & Chen, W. (2022b). Comparative study on explosion characteristics of hydrogen and gasoline vapor in a semi-confined pipe based on large eddy simulation. *Fuel*, *328*, 125334. https://doi.org/https://doi.org/10.1016/j.fuel.2022.125334

Liu, Li, X., Li, M., & Xiao, H. (2023). Flame acceleration and DDT in a channel with fence-type obstacles: Effect of obstacle shape and arrangement. *Proceedings of the Combustion Institute*, *39*(3), 2787-2796. https://doi.org/https://doi.org/10.1016/j.proci.2022.08.046

Liu, Zhang, Y., Niu, F., & Li, L. (2015). Study on the flame propagation and gas explosion in propane/air mixtures. *Fuel*, *140*, 677-684. https://doi.org/https://doi.org/10.1016/j.fuel.2014.09.123

Luo, G., Tu, J. Q., Qian, Y. L., Jin, K. K., Ye, T. J., Bai, Y., & Gao, S. (2022). Impacts of rectangular obstacle lengths on premixed methane–air flame propagation in a closed tube. *Combustion, Explosion, and Shock Waves*, *58*(1), 10-21. https://doi.org/10.1134/S0010508222010026

Momferatos, G., Giannissi, S. G., Tolias, I. C., Venetsanos, A. G., Vlyssides, A., & Markatos, N. (2022). Vapor cloud explosions in various types of confined environments: CFD analysis and model validation. *Journal of Loss Prevention in the Process Industries*, *75*, 104681. https://doi.org/https://doi.org/10.1016/j.jlp.2021.104681

Na'inna, A. M., Somuano, G. B., Phylaktou, H. N., & Andrews, G. E. (2015). Flame acceleration in tube explosions with up to three flat-bar obstacles with variable obstacle separation distance. *Journal of Loss Prevention in the Process Industries*, *38*, 119-124. https://doi.org/https://doi.org/10.1016/j.jlp.2015.08.009

Na'inna, A. M., Phylaktou, H. N., & Andrews, G. E. (2014). Effects of obstacle separation distance on gas explosions: the influence of obstacle blockage ratio. *Procedia Engineering*, *84*, 306-319. https://doi.org/https://doi.org/10.1016/j.proeng.2014.10.439

Nakahara, K., Yoshida, A., & Nishioka, M. (2021). Experiments and numerical simulation on the suppression of explosion of propane/air mixture by water mist. *Combustion and Flame*, *223*, 192-201. https://doi.org/https://doi.org/10.1016/j.combustflame.2020.09.014

Nguyen, T., Strebinger, C., Bogin, G. E., & Brune, J. (2021). A 2D CFD model investigation of the impact of obstacles and turbulence model on methane flame propagation. *Process Safety and Environmental Protection*, *146*, 95-107. https://doi.org/https://doi.org/10.1016/j.psep.2020.08.023

Olugbemide, D. I. (2022). A CFD study of the effects of pipe bending angle on pressure piling in coal dust explosions in interconnected vessels. *Fire Safety Journal*, *128*, 103540. https://doi.org/https://doi.org/10.1016/j.firesaf.2022.103540

Pan, C., Wang, X., Sun, H., Zhu, X., Zhao, J., Fan, H., & Liu, Y. (2022). Large-eddy simulation and experimental study on effects of single-dual sparks positions on vented explosions in a channel. *Fuel*, *322*, 124282. https://doi.org/https://doi.org/10.1016/j.fuel.2022.124282

Ponizy, B., Claverie, A., & Veyssière, B. (2014). Tulip flame - the mechanism of flame front inversion. *Combustion and Flame*, *161*(12), 3051-3062. https://doi.org/https://doi.org/10.1016/j.combustflame.2014.06.001

Qiao, Z., Ma, H., & Li, C. (2023). Influence of change in obstacle blocking rate gradient on LPG explosion behavior. *Arabian Journal of Chemistry*, *16*(2), 104496. https://doi.org/https://doi.org/10.1016/j.arabjc.2022.104496

Qin, J., Tan, Y., Wang, Z., & Pan, P. (2012). Experimental study of the effect of the shape of obstacles in pipelines on gas explosions. *Coal science and Technology*, *40*(2), 3. https://doi.org/10.1016/j.jlp.2022.104824.

Raj, R., Kumar Singh, D., & Vachan Tirkey, J. (2023). Performance simulation and optimization of SI engine fueled with peach biomass-based producer gas and propane blend. *Thermal Science and Engineering Progress*, *41*, 101816. https://doi.org/https://doi.org/10.1016/j.tsep.2023.101816

Ruipengyu, Malalasekera, W., Ibrahim, S., & Masri, A. (2021). An LES-DFSD study of transient premixed propane/air flames propagating past obstacles. *Fuel*, *302*, 121099. https://doi.org/https://doi.org/10.1016/j.fuel.2021.121099

Saeid, Hosein, M., Khadem, J., & Emami, S. (2021). Numerical investigation of the mechanism behind the deflagration to detonation transition in homogeneous and inhomogeneous mixtures of H2-air in an obstructed channel. *International Journal of Hydrogen Energy*, *46*(41), 21657-21671. https://doi.org/https://doi.org/10.1016/j.ijhydene.2021.04.006

Shen, X., Zhang, C., Xiu, G., & Zhu, H. (2019). Evolution of premixed stoichiometric hydrogen/air flame in a closed duct. *Energy*, *176*, 265-271. https://doi.org/https://doi.org/10.1016/j.energy.2019.03.193

Sheng, Z., Yang, G., Gao, W., Li, S., Shen, Q., & Sun, H. (2023). Study on the dynamic process of premixed hydrogen-air deflagration flame propagating in a closed space with obstacles. *Fuel*, *334*, 126542. https://doi.org/https://doi.org/10.1016/j.fuel.2022.126542

Signetti, S., Klomfass, A., Riedel, W., Putzar, R., & Heine, A. (2023). Simulation of blast propagation and structural effects of accidental hydrogen-air-mixture explosion in a two-stage light-gas gun laboratory for hypervelocity impact experiments. *Journal of Loss Prevention in the Process Industries*, *85*, 105138. https://doi.org/https://doi.org/10.1016/j.jlp.2023.105138

Tartandyo, R. A., Ginting, B. M., & Zulfan, J. (2023). Scale effects investigation in physical modeling of recirculating shallow flow using large eddy simulation technique. *Journal Of Applied Fluid Mechanics*, *17*(1), 43-59. https://doi.org/10.47176/jafm.17.1.1980

Ustolin, F., Tolias, I. C., Giannissi, S. G., Venetsanos, A. G., & Paltrinieri, N. (2022). A CFD analysis of liquefied gas vessel explosions. *Process Safety and Environmental Protection*, *159*, 61-75. https://doi.org/https://doi.org/10.1016/j.psep.2021.12.048

Wang, & Ma. (2021a). Explosion dynamics of hydrogen-air mixtures in a flat vessel filled with annular obstacles. *Fuel*, *298*(4), 120835. https://doi.org/10.1016/j.fuel.2021.120835.

Wang, & Ma. (2021b). Explosion dynamics of hydrogen-air mixtures in a flat vessel filled with annular obstacles. *Fuel*, *298*, 120835. https://doi.org/https://doi.org/10.1016/j.fuel.2021.120835

Wang, Yang, P., Yi, W., Luo, Z., Cheng, F., Ding, X., Kang, X., Feng, Z., & Deng, J. (2022a). Effect of obstacle shape on the deflagration characteristics of premixed LPG-air mixtures in a closed tube. *Process Safety and Environmental Protection*, *168*, 248-256. https://doi.org/https://doi.org/10.1016/j.psep.2022.09.079

Wang, Yi, W., Liang, H., Yang, P., Luo, Z., Sun, L., Cheng, F., Kang, X., Feng, Z., & Deng, J. (2023a). Experimental research on the pressure and flame propagation behaviors of LPG-air mixtures in a double obstructed tube. *Journal of Loss Prevention in the Process Industries*, *82*, 104979.

https://doi.org/https://doi.org/10.1016/j.jlp.2023.104979

Wang, Q., Luo, X., Li, Q., Rui, S., Wang, C., & Zhang, A. (2022b). Explosion venting of hydrogen-air mixture in an obstructed rectangular tube. *Fuel*, *310*, 122473. https://doi.org/https://doi.org/10.1016/j.fuel.2021.122473

Wang, Z., Yin, Y., Li, S., Xu, Y., Li, L., & Li, G. (2023b) Analysis of near-wall coherent structure of spiral flow in circular pipe based on large eddy simulation. *Journal Of Applied Fluid Mechanics*, *17*(1), 105-115. https://doi.org/10.47176/jafm.17.1.2038

Lv, X., Zheng, L., Zhang, Y.,Yu, M., & Su, Y. (2016). Combined effects of obstacle position and equivalence ratio on overpressure of premixed hydrogen-air explosion. International Journal of Hydrogen Energy, 41(39), 17740-17749. https://doi.org/10.1016/j.ijhydene.2016.07.263.

Xiu, Z., Liu, Z., Li, P., Li, M., Zhao, Y., Fan, T., & Yuan, J. (2023a). Effects of combined obstacles on deflagration characteristics of hydrogen-air premixed gas. *International Journal of Hydrogen Energy*, *48*(79), 31008-31021. https://doi.org/https://doi.org/10.1016/j.ijhydene.2023.04.251

Xiu, Z., Liu, Z., Li, P., Li, M., Zhao, Y., Fan, T., & Yuan, J. (2023b). Progress of research on the effect of non-uniform premixing on hydrogen and methane explosion characteristics. *Process Safety and Environmental Protection*, *180*, 856-867. https://doi.org/https://doi.org/10.1016/j.psep.2023.10.056

Xu, C., Cong, L., Yu, Z., Song, Z., & Bi, M. (2015). Numerical simulation of premixed methane-air deflagration in a semi-confined obstructed chamber. *Journal of Loss Prevention in the Process Industries*, *34*(Null). https://doi.org/10.1016/j.jlp.2015.02.007.

Yang, X., Krul, K., & Sims, D. (2022). Uncovering coal mining accident coverups: An alternative perspective on China's new safety narrative. *Safety Science*, *148*, 105637. https://doi.org/https://doi.org/10.1016/j.ssci.2021.105637

Yang, K., Miao, H., Ji, H., Chen, S., Xing, Z., Jiang, J., Zheng, K., & Liu, G. (2024) Experimental study on the coupling effect of heptafluoropropane and different arrangement of obstacles on methane-air explosion. *Fuel*, *358*, 130204. https://doi.org/https://doi.org/10.1016/j.fuel.2023.130204

Yu, M., Zheng, K., & Chu, T. (2016). Gas explosion flame propagation over various hollow-square obstacles. *Journal of Natural Gas Science and Engineering*, *30*, 221-227. https://doi.org/https://doi.org/10.1016/j.jngse.2016.02.009

Zhang, C., Dong, H., Shang, S., Zhang, K., Zhang, Z., & Gao, W. (2023). Investigation of the length-to-diameter ratio of ducts effect on the oscillation propagation behavior and vented characteristics for propane-air vented explosions. *Journal of Loss Prevention in the Process Industries*, *86*, 105186. https://doi.org/https://doi.org/10.1016/j.jlp.2023.105186

Zhang, K., Du, S., Chen, H., Wang, J., Zhang, J., Guo, Y., & Guo, J. (2022). Effect of hydrogen concentration on the vented explosion of hydrogen–air mixtures in a 5-m-long duct. *Process Safety and Environmental Protection*, *162*, 978-986. https://doi.org/https://doi.org/10.1016/j.psep.2022.05.003

Zhang, Z., Wang, H., Wang, Z., Tian, W., & Wang, Z. (2021). The effect of orifice plates with different shapes on explosion propagation of premixed methane–air in a semi-confined pipeline. *Journal of Loss Prevention in the Process Industries*, *71*, 104498. https://doi.org/https://doi.org/10.1016/j.jlp.2021.104498

Zhao, X., Wang, J., Gao, L., Wang, X., & Zhu, Y. (2022). Flame acceleration and onset of detonation in inhomogeneous mixture of hydrogen-air in an obstructed channel. *Aerospace Science and Technology*, *130*, 107944. https://doi.org/https://doi.org/10.1016/j.ast.2022.107944

Zheng, K., Jia, Q., Ma, Z., Xing, Z., Hao, Y., & Yu, M. (2023). Experimental and numerical investigation on the premixed methane/air flame propagation in duct with obstacle gradients. *Process Safety and Environmental Protection*, *178*, 893-904. https://doi.org/https://doi.org/10.1016/j.psep.2023.08.077

Zimont, V. L., & Battaglia, V. (2005). Joint RANS/LES approach to premixed flames modelling in the context of the TFC combustion model. In W. Rodi & M. Mulas (Eds.), *Engineering Turbulence Modelling and Experiments 6* (pp. 905-914). Elsevier Science B.V. https://doi.org/https://doi.org/10.1016/B978-008044544-1/50087-X